Dopant-Induced Modification of Active Site Structure and Surface Bonding Mode for High-Performance Nanocatalysts: CO Oxidation on Capping-free (110)-oriented CeO$_2$:Ln (Ln = La−Lu) Nanowires

Jun Ke,[†] Jia-Wen Xiao,[†,⊥] Wei Zhu,[†,⊥] Haichao Liu,*[,‡] Rui Si,[§] Ya-Wen Zhang,*[,†] and Chun-Hua Yan*[,†]

[†]Beijing National Laboratory for Molecular Sciences, State Key Laboratory of Rare Earth Materials Chemistry and Applications, PKU-HKU Joint Laboratory in Rare Earth Materials and Bioinorganic Chemistry and [‡]Beijing National Laboratory for Molecular Sciences, State Key Laboratory for Structural Chemistry of Stable and Unstable Species, College of Chemistry and Molecular Engineering, Peking University, Beijing 100871, China

[§]Shanghai Synchrotron Radiation Facility, Shanghai Institute of Applied Physics, Chinese Academy of Sciences, Shanghai 201204, China

Ⓢ *Supporting Information*

ABSTRACT: Active center engineering at atomic level is a grand challenge for catalyst design and optimization in many industrial catalytic processes. Exploring new strategies to delicately tailor the structures of active centers and bonding modes of surface reactive intermediates for nanocatalysts is crucial to high-efficiency nanocatalysis that bridges heterogeneous and homogeneous catalysis. Here we demonstrate a robust approach to tune the CO oxidation activity over CeO$_2$ nanowires (NWs) through the modulation of the local

structure and surface state around Ln$_{Ce}'$ defect centers by doping other lanthanides (Ln), based on the continuous variation of the ionic radius of lanthanide dopants caused by the lanthanide contraction. Homogeneously doped (110)-oriented CeO$_2$:Ln NWs with no residual capping agents were synthesized by controlling the redox chemistry of Ce(III)/Ce(IV) in a mild hydrothermal process. The CO oxidation reactivity over CeO$_2$:Ln NWs was dependent on the Ln dopants, and the reactivity reached the maximum in turnover rates over Nd-doped samples. On the basis of the results obtained from combined experimentations and density functional theory simulations, the decisive factors of the modulation effect along the lanthanide dopant series were deduced as surface oxygen release capability and the bonding configuration of the surface adsorbed species (i.e., carbonates and bicarbonates) formed during catalytic process, which resulted in the existence of an optimal doping effect from the lanthanide with moderate ionic radius.
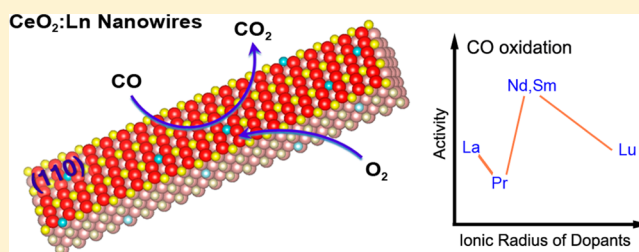
■ INTRODUCTION

Rational design and empirical construction of robust active centers atom by atom are vital for the development of atom-efficient catalysis.[1] From this aspect, nanocatalysts have the advantages of both homogeneous and heterogeneous catalysts because of their controllable surfaces.[2] Based on the nanocrystals with well-defined shapes[3] and monodisperse sizes,[3d,4] the conventional way to control their active sites is the modification of their surface structures including integrating or assembling interfaces,[5] producing phase separation and surface segregation,[6] anchoring additional active components,[7] and engineering defect structures.[8] In most cases, the variation of catalytic performance can be attributed to the distinctive properties of significantly altered active sites or compositions.[3−8] However, toward achieving enzyme-like or single-site-like nanocatalysts with high efficiency and specificity,[2a,9] the fine-tuning of the local structure (e.g., bonding configuration, coordination number, and defect clustering) around certain active centers and the associated surface bonding behaviors are essential for optimizing catalyst performance of the catalyst

with maximized numbers of accessible active sites, which remains difficult for most of nanocatalysts. In the latest years, more and more studies on nanocatalysis indicate that single product model reactions (e.g., CO oxidation to CO$_2$, as an important benchmark reaction in catalysis) on model nanocatalysts with well-defined exposed facets, homogeneous chemical composition, and pure crystalline phases are the most straightforward approach for revealing the structure−function correlation at the atom level so as to comprehend the underlying principles behind the improved catalytic efficiencies for the nanocatalysts, which is critically important for the rational design and development of a more robust single component and even multicomponent catalyst for high-efficiency nanocatalysis.[10,7b]

Ceria has been massively used as promoters of three-way catalysts in automotive pollution control and has also demonstrated potential in important industrial catalytic

processes including water−gas shift reaction and many organic reactions based on its high redox and acid−basic catalytic reactivity.[11] Investigation on the catalytic mechanism referring to oxygen capacity has revealed that lattice oxygen plays an important role during the catalytic process for ceria.[11a,12] To improve the catalytic performance, control of shape, size, surface defects, and dopants has been exploited to modify the surface structures of CeO_2 nanomaterials.[13] Several kinds of ceria nanocrystals with typical exposed facets and surface structures (e.g., (110)-, (100)-, and (111)-exposed) have been carefully studied for understanding their morphology effects on the catalytic performances in CO oxidation reaction.[12,13a] Among the shape-tunable ceria nanocrystals (e.g., zero-dimensional (0D) dots and spheres, one-dimensional (1D) wires and rods, two-dimensional (2D) plates and sheets, and three-dimensional (3D) cubes and polyhedrons), 1D nanowires (NWs) have been demonstrated to possess rather high-catalytic activities for CO oxidation because they expose rough and active (110) facets, on which oxygen defects are easy to form, that in turn facilitate the migration of lattice oxygen for oxidation of adsorbed CO intermidiates.[12,13a]

More recently, theoretical simulations have also been carried out to help to design new ceria-based structures with improved CO oxidation activities by doping foreign cations into the parent oxide host.[14] Study on CeO_2:La has found that La dopant might increase the oxygen release ability, strengthen CO adsorption on surfaces, and thus considerably activate the CO oxidation reaction from active centers around the La_{Ce}' defects.[14a−c] Experimental studies on CeO_2:Ln (Ln = La, Eu, Gd) nanopowders have revealed that the doping of various lanthanides into CeO_2 lattice could enhance CO oxidation activities.[15] As is known, well-defined exposed facets and similar surface structures are prerequisites for executing model catalytic studies on such Ln-doped ceria nanomaterials, so as to reveal the intrinsic catalytic behaviors of doping created active centers and to gain insights from theoretical simulations with simplified models. So far, a systematic study on uniformly doped CeO_2 nanocrystals with serial lanthanides based on controllable synthesis and the reliance of their catalytic activity on Ln series for certain model reaction was rarely reported both experimentally and theoretically. This might be because of the difficulty in controllable synthesis of CeO_2:Ln nanocrystals, especially highly active 1D NWs, led by the differences in valence and ionic radii between Ln(III) and Ce(IV).

In this article, we report controllable synthesis of Ln-doped (110)-oriented CeO_2 NWs from La to Lu and their CO oxidation reactivity by experimentations and density functional theory (DFT) calculations. The CeO_2:Ln NWs were prepared through a facile hydrothermal treatment based on the redox ability of Ce(III)/Ce(IV) couple in the absence of organic capping agents. More importantly, their turnover rates for CO oxidation were demonstrated to be highly sensitive to the ionic radius of Ln dopant through its modulation on the oxygen vacancy formation ability in ceria lattices and on the surface adsorbed species (i.e., carbonates and bicarbonates) formed in the catalytic process.

■ EXPERIMENTAL SECTION

CeO_2:Ln NWs were prepared through hydrothermal process with commercially available reagents. $CeCl_3$·$7H_2O$ (99%, Sinopharm Chemical Corp., China), lanthanide oxides (>99.5%, Fangzheng Xindong'an Corp., China), NaOH (A.R., Beijing Chemical Corp.,

China), and NaCl (A.R., Beijing Chemical Corp., China) were used as received.

Synthesis of CeO_2:Ln NWs. $LnCl_3$ was prepared by dissolving lanthanide oxides in hydrochloric acid (1:1 in volume). 0.675 mmol of $CeCl_3$·$7H_2O$, 0.523 g of NaCl, and 1000 μL of $LnCl_3$ (0.075 mol·L^{-1}) solution (with 0.40 mol·L^{-1} of HCl) were dissolved in 6 mL of water and then mixed with 7.5 mL of NaOH solution (12.0 mol·L^{-1}). The total volume of the suspension was adjusted to 15 mL. The suspension was transferred to a 25 mL Teflon-lined stainless steel autoclave and heated at 180 °C for 24 h. The products were washed with water three times, dried at 70 °C, and then calcined at 300 °C for 1 h.

Instrumentation. X-ray diffraction (XRD) patterns were obtained on a D/MAX-2000 diffractometer (Rigaku, Japan) with Cu−Kα radiation. Lattice parameter was calculated with the LAPOD code. Inductively coupled plasma-atomic spectroscopy (ICP-AES) analysis was performed on a Profile Spec ICP-AES spectrometer (Leeman, U.S.A.). X-ray photoelectron spectroscopy (XPS) analysis was performed on an Axis Ultra XPS spectrometer (Kratos, U.K.) with 225 W of Al Kα radiation. The C 1s line at 284.8 eV was used to calibrate the binding energies (BE). Transmission electron microscopy (TEM) images were obtained on a JEOL JEM2100 TEM (Japan) operated at 200 kV. High-resolution TEM (HRTEM), high-angle annular dark-field scanning transmission electron microscopy (HAADF-STEM), and energy dispersive X-ray spectroscopy (EDS) elemental mapping were performed on a FEG-TEM (JEM2100F, JEOL, Japan) operated at 200 kV. Before the TEM examination, the samples were prepared by dispersing the products in water and drying a droplet of the suspension on copper grids coated with holey carbon membranes. Raman spectra were collected on a Jobin−Yvon HR800 Laser Raman Microscope with 325 nm laser excitation. Brunauer−Emmett−Teller (BET) specific surface area of the samples calcined at 150 °C in vacuum was measured via nitrogen adsorption at 77 K on an ASAP-2010 analysis system (Micromeritics, U.S.A.). Ce K-edge EXAFS analysis was performed on the BL14W1 beamline of Shanghai Synchrotron Radiation Facility (SSRF) operated at 3.5 GeV under "top-up" mode with current of 220 mA. Gd, Ho, and Lu L_3-edge absorption spectra were obtained on the 1W2B beamline of Beijing Synchrotron Radiation Facility (BSRF) operated at 2.2 GeV with injection currents of 300−500 mA. Bulk CeO_2 and Ln_2O_3 were used as reference samples and measured in transmission mode. For nanowire samples, Ce K-edge absorption was measured in transmission mode, while Gd, Ho, and Lu L_3-edge absorption was measured in fluorescence mode. Athena and Artemis codes were used to extract the data and to fit the curves with the reported model,[16] respectively. The Fourier transformed curves were fitted in real space with $\Delta k = 2-9$ $Å^{-1}$ and $\Delta R = 1.2-2.5$ Å for Ce (k^2 weighted) and with $\Delta k = 2-9$ $Å^{-1}$ and $\Delta R = 1.5-2.7$ Å for Ln (k^3 weighted). Temperature-programmed reduction with H_2 (H_2-TPR) analysis was performed by ramping 30 mg of the sample up to 700 °C (10 °C/min) in H_2 (5 vol %)/He flow (40 mL/min). H_2 consumption was analyzed by a thermoconductivity detector (TCD). IR spectra were obtained with a TENSOR 27 spectrometer (Bruker, German) in diffuse reflectance mode (DRIFTS). Samples in the Praying Mantis DRIFTS cell were exposed to CO (0.5 vol%)/O_2 (5 vol%)/He flow (40 mL/min). Before the H_2-TPR and IR analyses, the samples were pretreated in flowing air at 300 °C for 30 min.

Catalytic Tests. The catalytic performance of CeO_2:Ln NWs on CO oxidation was measured in a fixed bed reactor. 100 mg of each sample was placed in a quartz tube with the gas speed of 40 mL/min. The feed gas contained 1 vol% CO, 20 vol% O_2, and balance He. The effluent gas compositions were analyzed by an online gas chromatograph (Agilent 7890A, U.S.A.) with a carbon molecular sieve column (Carboxen 1000, Supelco, U.S.A.) and TCD.
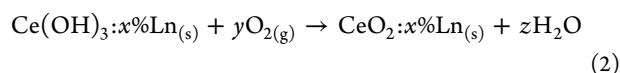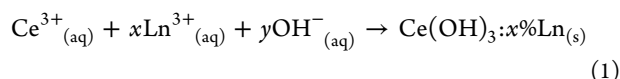
First-Principles Calculations. DFT calculation was executed with the VASP package. Spin-polarized Kohn−Sham equations were expanded into plain waves. The exchange−correlation energy functional was described in the Perdew−Burke−Ernzerhof (PBE) generalized gradient approximation (GGA). In the Brillouin zone, only the properties at the Gamma point were considered. The atoms were presented by projector augmented wave (PAW) pseudopotentials. The

kinetic energy cutoff for the plane-wave basis set was 500 eV. (110) surface exposed $3 \times 3 \times 5$ ceria supercells with two fixed layers and 15 Å of vacuum were built for the simulation. Five eV of U was added on Ce 4f orbital.[14c,17] To simulate CeO$_2$:Ln, one Ce in each level was replaced by an Ln atom. Only three of the 4f, 5d, and 6s electrons of trivalent Ln were treated as valence electrons, and the rest of the 4f electrons were frozen into the core. To simulate valence changeable Pr, its 4f and 6s electrons were treated as valence electrons, and the same 5 eV of U was added on its 4f orbital.[13g,18] Each structure was relaxed until the residual force was <0.02 eV/Å.

■ RESULTS AND DISCUSSION

Preparation and Characterization of the CeO$_2$:Ln NWs. Ln (10 mol %) doped CeO$_2$ NWs were obtained with a modified hydrothermal approach based on the coprecipitation of lanthanide cations in the coexistence of NaOH and NaCl without any organic capping ligands.

As is known, the solubility product of Ln(OH)$_3$ (2.0×10^{-19}–1.9×10^{-24} for La(OH)$_3$–Lu(OH)$_3$) is much closer to that of Ce(OH)$_3$ (1.6×10^{-20}) than that of Ce(OH)$_4$ (2×10^{-48}).[19] The difference of ionic radius between Ln^{3+} (116–97.7 pm for La^{3+}–Lu^{3+}) and Ce^{3+} (114.3 pm) is no more than 15%.[20] Considering the above similarity of Ce^{3+} and Ln^{3+} in valence, ionic radius, and solubility product during aqueous precipitation, in this work, Ln^{3+} could be quantitatively doped into Ce(OH)$_3$ intermediates (Figure S1 in Supporting Information) to form Ce(OH)$_3$:Ln NWs based on the redox ability of Ce(III)/Ce(IV). Then, the as-made Ce(OH)$_3$:Ln NWs were oxidized and dehydrated in open air, and CeO$_2$:Ln NWs were finally obtained. Such preparation process could be described with the following equations:

$$Ce^{3+}_{(aq)} + xLn^{3+}_{(aq)} + yOH^-_{(aq)} \rightarrow Ce(OH)_3:x\%Ln_{(s)} \tag{1}$$

$$Ce(OH)_3:x\%Ln_{(s)} + yO_{2(g)} \rightarrow CeO_2:x\%Ln_{(s)} + zH_2O \tag{2}$$

In this approach, the NWs formed their shapes from the preferable growth of 1D Ce(OH)$_3$ intermediates with hexagonal structure (Figure S1 in SI). Different from previous reports on the hydrothermal preparation of CeO$_2$ nanorods and NWs, the use of small amount of NaCl in the present synthesis could make the Ln-doped Ce(OH)$_3$ NWs grow more uniformly and anisotropically with high aspect ratios. Upon calcining at 300 °C for 1 h, the Ce(OH)$_3$:Ln NWs could transform into CeO$_2$:Ln NWs with good chemical homogeneity for further catalytic measurements.

The XRD patterns (Figure S2 in SI) of the doped samples were similar to that of undoped ceria (JCPDS 04-0593). There was no other obvious diffraction peaks attributable to other components or phases. The lattice parameter of CeO$_2$:La–CeO$_2$:Lu NWs decreased from 546 to 541 pm (Table S1 in SI), suggesting the altered lattice distortion in the nanocrystals due to the change of Ln–O bond length resulted from the decreasing ionic radius of the dopants. XPS results showed that the valences of the Ln dopants were trivalent (Table S1 and Figures S3 and S4 in SI) and that the amount of the dopants in the surface layers of each CeO$_2$:Ln sample was around 10%. It agreed with the bulk value obtained from ICP-AES. According to the Ce 3d spectra obtained from XPS measurements, the ratio of Ce^{3+} in each Ln-doped sample decreased to about zero, while 8% of Ce was trivalent in undoped CeO$_2$ sample. There was no Cl species found in the samples according to XPS analysis (Figure S3a in SI), indicating that the intrinsic (110)

surfaces of the NWs might be majorly exposed. However, some hydroxyls might exist on the surfaces of the NWs, as deduced from the appearance of the shoulder peaks at 531 and 533 eV in the XPS O 1s spectra (Figure S3e in SI).

TEM images showed that the morphology of Ln-doped CeO$_2$ appeared as nanowires. From CeO$_2$:La to CeO$_2$:Gd, the sizes of the NWs were similar to that of the undoped ones (Figure S5 and Table S1 in SI). The aspect ratio decreased from about 500 to 10 when the dopants varied from Gd to Lu. During the growth process of ceria NWs, the difference of ionic radius between Ln^{3+} and Ce^{3+} (114.3 pm) in the Ce(OH)$_3$ intermediates increased from La^{3+} (116 pm) to Lu^{3+} (97.7 pm). The increasing misfit of heavy Ln dopants to the host Ce^{3+} cations might increase the surface lattice strain of the crystals when crystallizing,[21] leading to the decreasing growth rate for heavy Ln-doped CeO$_2$ NWs. Previous study has shown that the size of CeO$_2$ nanocrystals, particularly the length of one-dimensional nanorods, has a positive relation to the growth rate.[13b] Thus, the size of CeO$_2$:Ln NWs decreased with the increasing ionic radius of the dopant. Because the growth along the side faces of the NWs was restrained, the growth along the axis direction was much more affected. Under this condition, the length decreased more greatly than the width did for heavy Ln-doped NWs, leading to the decreasing aspect ratio along Gd–Lu. The BET specific surface area was around 34–44 m^2·g^{-1} for La–Gd-doped and undoped ceria (Table S2 in SI), and it increased from CeO$_2$:Gd to CeO$_2$:Ho and was around 72–84 m^2·g^{-1} for Ho–Lu-doped samples. This result agreed with the variation trend of the NWs sizes measured from the TEM images.

Figure 1 shows the TEM, HRTEM, and EDS elemental mapping images of some typical samples. Most of the NWs in HRTEM images exposed (110) facets. EDS elemental mapping images obtained from HAADF-STEM showed that the distribution of the dopants was uniform in the nanocrystals, indicating good chemical homogeneity of the doped samples. There were some observable black dots on the surfaces of the CeO$_2$:Ln NWs from the HRTEM images (Figure 1b,d), which has also been observed on undoped CeO$_2$ nanorods due to the coordinatively unsaturated sites on (110) surfaces.[12a,b]

Oxygen defects in the NWs samples were evaluated with UV (325 nm) Raman analysis (Figure S6 in SI). The intensity ratio of D mode at 586 cm^{-1} to F$_{2g}$ mode at 456 cm^{-1} ($I(D)/I(F_{2g})$) increased from 1.1 to 1.5 for La–Lu-doped CeO$_2$, suggesting the increasing density of surface oxygen defects in heavy Ln-doped samples.[12b] Considering that the amount of trivalent cations in each sample was similar according to XPS analyses, the variation of $I(D)/I(F_{2g})$ should be attributed to Frenkel-type oxygen defects in CeO$_2$:Ln.[12b] The increased oxygen defects in heavy Ln-doped nanocrystals might owe its origin to the increased misfit of dopants in Ce(OH)$_3$:Ln intermediates during their growth, leading to increased interstitial defects in CeO$_2$:Ln after oxidation.[21]

EXAFS analysis was carried out to examine the local structure around the active centers of the NWs. Considering the overlapping between the L$_3$ edge of Ce and light Ln in energy, we chose the L$_3$ edge of Gd, Ho, Lu and the K edge of Ce to perform the test. Interatomic distance (R) in the first coordination shell obtained from real space data fitting (Figure S7 in SI) is summarized in Table 1 (see Table S3 for details). From Gd to Lu-doped NWs, R(Ln–O) value decreased from 237 to 233 pm, which was consistent with the changes in the ionic radius of the dopants and the calculated lattice parameter
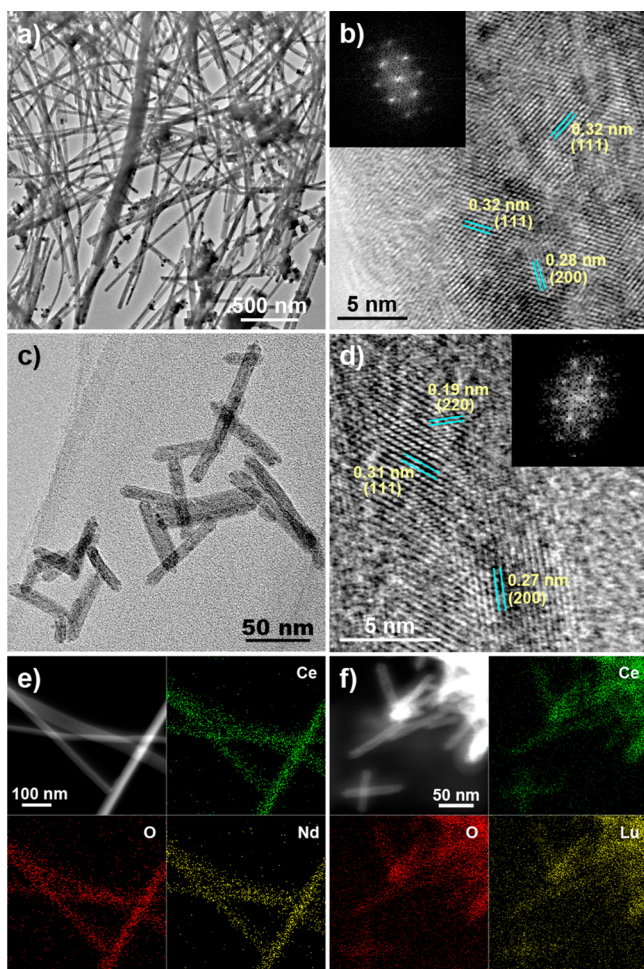
Figure 1. TEM (a,c), HRTEM (b,d), and HAADF-STEM EDS elemental mapping (e,f) images of CeO_2:Nd (a,b,e) and CeO_2:Lu nanocrystals (c,d,f). Insets in panels b and d are the fast Fourier transition analyses, indicating that (110) surfaces are exposed for both samples. In panels e and f, the up-left images are the HAADF-STEM images. The upper right and bottom left and right ones in panels e and f are the EDS elemental mapping images representing Ce, O, and the dopant (Nd for panel e and Lu for panel f), respectively. The images for other CeO_2:Ln samples were similar.

Table 1. EXAFS Parameters of CeO_2:Ln NWs

sample	shell	R (Å)^a	sample	shell	R (Å)
CeO_2	Ce–O	2.34	CeO_2:Ho	Ce–O	2.34
CeO_2:La	Ce–O	2.34	CeO_2:Lu	Ce–O	2.35
CeO_2:Pr	Ce–O	2.34	CeO_2:Gd	Gd–O	2.37
CeO_2:Nd	Ce–O	2.33	CeO_2:Ho	Ho–O	2.34
CeO_2:Gd	Ce–O	2.33	CeO_2:Lu	Lu–O	2.33

^{a}Uncertainty of the fitting was ±0.02 Å for the Gd–O shell and ±0.01 Å for the others.

obtained from XRD (Table S1). R(Ce–O) values kept almost unchanged in the doped samples on average and were similar to that (234 pm) in the undoped sample, suggesting that the structure disorder might be mainly localized around the dopants. The variation trend of R(Ln–O) values for light Ln-doped NWs should be similar. In CeO_2:Gd NWs, R(Gd–O) value (2.37 Å) was greater than that of R(Ce–O) (2.33 Å), indicating the lattice expansion around the dopants in light Ln-

doped samples. Similarly, very slight lattice contraction around the dopants might exist in heavy Ln-doped samples.

CO Oxidation Reactivities of the CeO_2:Ln NWs. To evaluate the lanthanide doping effect on the catalytic properties of CeO_2 NWs, we selected CO oxidation as a model reaction and investigated the variation of catalytic activity with Ln dopants. The temperature of half conversion (T_{50}) and the specific reaction rate at 200 °C are summarized in Table S2 in SI (CO conversion at 200 °C were below 15% for all the samples). Turnover frequency could be calculated according to theoretical surface oxygen density on (110) facets[22] (Figure 2).
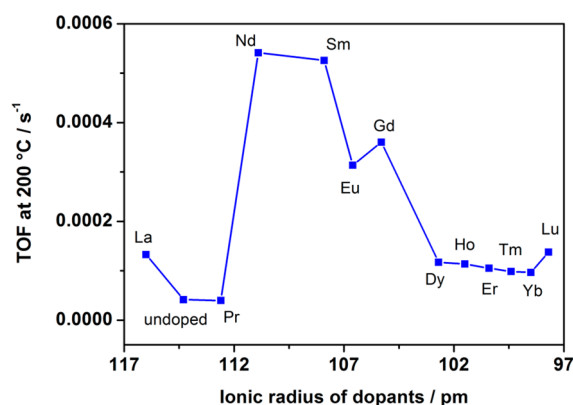

Figure 2. Catalytic activity for catalytic CO oxidation over CeO_2:Ln NWs and its relation to the ionic radius of the dopant. Error bounds were estimated to be within ±20%. Pr-doped and undoped ceria were placed according to the ionic radius of their trivalent cations for the convenience of comparison.

Differences at corners and edges could be ignored without changing the activity sequence because the morphology of each sample was similar. CeO_2:Ln NWs showed markedly improved catalytic activities than undoped ones. Nd- and Sm-doped samples gave the best catalytic performances. The present CeO_2:Nd NWs were more active (0.031 mmol·h^{-1}·m^{-2} at 200 °C) than the nanosized powders obtained from conventional coprecipitation method[15] (0.0030 mmol·h^{-1}·m^{-2} at 200 °C) probably because the NWs mainly exposed well-defined active (110) facets. With the decreasing ionic radius of dopants, TOF at 200 °C increased from 1.3×10^{-4} s^{-1} to 5.4×10^{-4} s^{-1} for CeO_2:La–CeO_2:Nd, then it decreased to 1.4×10^{-4} s^{-1} until CeO_2:Lu. Therein, the activity for CeO_2:Dy–CeO_2:Lu was very similar (between 1.0×10^{-4}–1.4×10^{-4} s^{-1}). T_{50} also showed similar sequence (Table S2 in SI). The catalytic activity of valence changeable Pr-doped NWs became worse than that expected on the trend line (Figure 2). To understand the complicated variation pattern of the CO oxidation activity for the CeO_2:Ln NWs, some representative Ln-doped and valence changeable Pr-doped samples were selected for further evaluations.
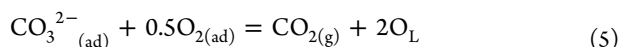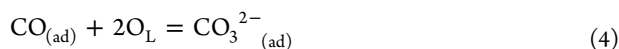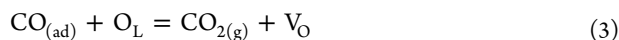
It is noted that the highly active CeO_2:Nd NWs did not show much loss of catalytic activity within several test periods (Figure S8 in SI). After catalytic tests, no obvious segregation of the dopants was observed for the CeO_2:Ln NWs according to the XRD, XPS, and EDS elemental mapping analysis results (Figure S9–S10 and Table S4 in SI). In addition, TEM and HRTEM images revealed that the (110) facets were still exposed for the NWs after catalytic reactions, but the surfaces became somewhat rougher for both doped and undoped samples (Figure S10 in SI). It was possibly due to the reconstruction of

certain sites on (110) surfaces to more stable and less active ones. Such phenomenon has been observed by thermal treatment under STM observation.[23] Therefore, in this work, to minimize the influences of surface reconstruction and/or phase segregation on the comparison of the catalytic activity of the NWs, all the catalytic treatments were performed below 350 °C.

Correlation between Catalytic Activity Variation and Ln Dopants. It is generally accepted that CO oxidation over ceria proceeds via Mars−van Krevelen mechanism.[11a,12a] CO removes the lattice oxygen, leading to the formation of oxygen vacancy (V_O), which is believed to be the rate-determining step. Then the oxygen vacancy is replenished with molecular oxygen through oxygen mobility.

As indicated by some literature reports,[11,12] the above catalytic steps can be affected by a lot of factors including morphology and surface planes, oxygen defects, oxygen mobility, and the variety of dopants. The effects of such factors on the observed activity sequence along the lanthanide series in the present catalytic process were estimated as below: (1) The facet effect could be excluded because the as-prepared CeO_2:Ln NWs had very similar morphologies with mainly exposed (110) facets; (2) although heavy Ln-doped CeO_2:Ln NWs had more intrinsic oxygen defects as shown by Raman spectra (which has been previously suggested to provide enhanced oxygen mobility during CO oxidation),[12b] they did not display corresponding improvements in catalytic activities (Figure 2), indicating an ignorable role of the oxygen defects in changing the activity sequence; (3) when the O_2 concentration was doubled or halved (10%−40%), TOF was not affected (Figure S11 in SI). For the same reason, Ce(III) proportion was found to be about zero after catalysis for all the samples from XPS Ce 3d spectra (Table S4 in SI). These results suggested that the oxygen replenishment and migration were relatively fast steps in the present oxygen-rich conditions, and thus should not dominate the activity sequence; (4) The roles of reactive species such as peroxides (O_2^{2-}) or superoxides (O_2^-) should be minimal because they are likely unstable in the temperature range of CO oxidation tests we performed (below 573 K), as proposed by previous spectroscopy studies.[12b] Therefore, we deduced that the variety of Ln dopants among the above was the dominant factor in determining the catalytic performances of the CeO_2:Ln NWs by the CO oxidation steps.

For CO oxidation to CO_2 over CeO_2 nanomaterials, two main reaction pathways have been previously suggested:[12a,24] CO direct oxidation with lattice (L) oxygen (eq 3) and surface process involving the formation and conversion of adsorbed (ad) carbonates species (eqs 4 and 5).

$$CO_{(ad)} + O_L = CO_{2(g)} + V_O \tag{3}$$

$$CO_{(ad)} + 2O_L = CO_3{}^{2-}{}_{(ad)} \tag{4}$$

$$CO_3{}^{2-}{}_{(ad)} + 0.5O_{2(ad)} = CO_{2(g)} + 2O_L \tag{5}$$

In this work, for CO oxidation over (110)-oriented CeO_2:Ln NWs, V_O formation ability and the bonding modes of adsorbed species generated from the reaction between CO and surface sites of the NWs were regarded as the two key factors in governing the catalytic activities by these two pathways.

Formation Ability of Oxygen Vacancies. H_2-TPR tests were carried out to reveal the property of V_O formation for the CeO_2:Ln NWs. In Figure 3 and Figure S12, the H_2
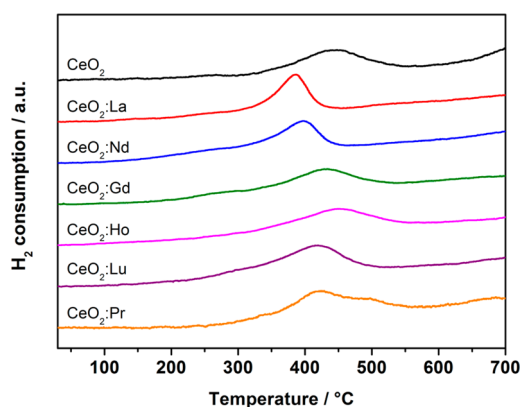

Figure 3. H_2-TPR analysis over some typical CeO_2:Ln samples.

consumption peaks at 380−580 °C were ascribed to the removal of surface oxygen.[25] Most of CeO_2:Ln NWs were more reductive than undoped one. The reducibility decreased from La-doped to Ho-doped samples and increased from Ho-doped to Lu-doped samples. Multivalent Pr-doped ceria NWs were relatively less reductive on average. CeO_2:Pr NWs showed a broad peak that covered the range of both Nd-doped and undoped ceria. The shoulder peak at 500 °C suggested the surface heterogeneity of microstructure for the CeO_2:Pr NWs;[15] whereas, such a case was not found for the other trivalent Ln-doped samples. It might be attributed to the special +3/+4 valence changeability of Pr among Ln dopants during synthesis. Experimentally, it was observed that both Pr and the other Ln-doped Ce(OH)₃ intermediates exhibited white color. Then, Pr-doped intermediates became brown rapidly when exposed to air, while the adjacent Ln-doped and undoped samples turned into light yellow quite slowly. This result suggested that the heterogeneity in CeO_2:Pr were possibly induced by the valence changeability of Pr atoms during the oxidation stage in open air. Previous study has also indicated that Pr(OH)₃ nanorods could form with similar hydrothermal synthesis, and the valence changeability of Pr took effect during its conversion process into Pr_6O_{11} nanorods.[26]

The reducibility sequence of the NWs was in good agreement with that of the catalytic activity as described above except for CeO_2:La, indicating that oxygen vacancy formation was an important factor to affect the catalytic activity. Theoretical study has pointed out that the aliovalent dopants may cause a lack of one electron around each $Ln_{Ce}{}'$ defect. When the hole is located onto nearby surface oxygen ion, it may activate the oxygen and make it easier to be removed than that on the undoped stoichiometric ceria.[14c]

DFT calculation can help to understand the trend of V_O formation for trivalent Ln-doped CeO_2 NWs. Because CeO_2:Ln NWs mainly exposed (110) facets, we built (110) surface exposed ceria model to execute computational simulation. (110) facets are much more active than other facets according to previous both experimental and theoretical reports[11,12c,14c] so it was reasonable to suppose that the dopants on (110) facets might affect the catalytic property. In each level of the model, one Ce ion was replaced by an Ln ion with uniform distribution (Figure 4). In this model, the doping ratio was 11%. Charge compensating oxygen vacancies were not specially put in our model.[14a] Nonclassic defect compensation has been found in Ln-doped ceria,[27] leading to the positive value of V_O formation energy. Considering that oxygen replenishment was
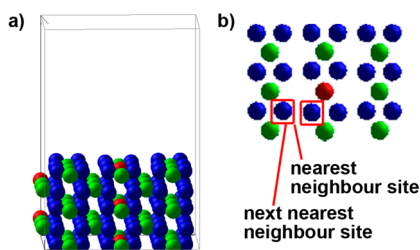
Figure 4. (a) Structure model of (110) surface exposed CeO_2:Ln built for DFT calculation. (b) View of the surface layer of the model. The two balls in red frames represent the oxygen at NN site and NNN site as marked in the picture. The green, blue, and red balls represent Ce, O, and the Ln dopant, respectively.

a fast step under oxygen-rich conditions in our catalytic tests, as long as V_O formation was positive in our system, charge compensating V_O would not be necessarily added. In addition, the existence of some hydroxyls on the surface in our model was unlikely a major factor to influence the oxygen release ability for our samples (see Table S5 in SI).

V_O formation energy (E_V) at the nearest-neighbor (NN) site and the next nearest-neighbor (NNN) site to the surface dopant were calculated through eq 6:

$$E_V = E(CeO_2 \text{with } V_O) + 1/2E(O_2) - E(CeO_2) \qquad (6)$$

Table S6 in SI and Figure 5 give the calculation results. E_V values for all the Ln(III)-doped ceria were lower than that for
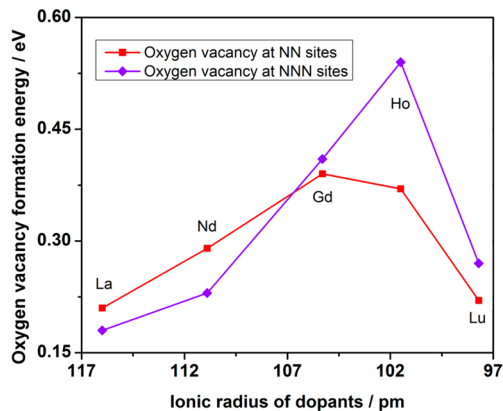

Figure 5. Oxygen vacancy formation energy for CeO_2:Ln on (110) surface and its relation to the ionic radius of the dopant. The red and violet marks represent the formation of oxygen vacancy at NN and NNN sites, respectively.

undoped one (1.54 eV). At NN site, E_V increased from 0.21 to 0.39 eV for La–Gd-doped ceria, and decreased from 0.37 to 0.22 eV for CeO_2:Ho–CeO_2:Lu. E_V at NNN site increased from 0.18 to 0.54 eV for La–Ho-doped ceria and then decreased to 0.27 eV for CeO_2:Lu. E_V at both sites showed similar variation trend along Ln dopants and showed an extreme point in each trend. The variation trend kept consistent with that of surface reducibility obtained from H_2-TPR measurements (Figure 3). For the model doped in the surface level with low doping ratio, E_V at NN site and E_V at NNN site showed monotonic and inverse trend along the Ln series (Table S7 in SI). Such difference was due to the long-range electronic effect of the Ln dopants with high doping concentration.[14a]

The relation between V_O formation ability and the structure distortion was estimated for 11% Ln-doped CeO_2. The average interatomic distance $R(Ce-O)$ in all levels was 235 pm for all samples (Table S6 in SI). Average $R(Ln-O)$ decreased from 243 to 236 to 232 pm for CeO_2:La–CeO_2:Gd–CeO_2:Lu, indicating the expansion around light Ln and slight contraction around heavy Ln, as also confirmed by the EXAFS results (Table 1). The turning point was at Gd–Ho. $R(Ce-O)$ and $R(Ln-O)$ in surface level had similar variation trends. The average $R(Ce-O)$ in surface level was 230 pm for all samples, and $R(Ln-O)$ decreased from 244 to 224 pm for La–Lu-doped ceria. The intersection was also at Gd–Ho, for which the V_O formation energy was also the highest. The decrease of E_V seemed to have a positive relation to the distortion around Ln dopant, irrespective of lattice expansion or contraction induced by the doping process.

As for valence changeable Pr-doped CeO_2, E_V at NN and NNN sites was 0.07 and −0.15 eV, respectively, which were close to those of trivalent Ln-doped ceria. It suggested that uniformly doped Pr could play very similar role as other trivalent ions. XPS Pr 3d spectra also indicated that trivalent Pr was dominant in CeO_2:Pr (Figure S4 in SI) because the peak represented Pr^{4+} was not obviously detected. However, the surface heterogeneity revealed for CeO_2:Pr NWs by H_2-TPR data (Figure 3) made it hard to build a suitable model to simulate, and was the most possible factor in limiting the activation effect of oxygen vacancies for this sample. Consequently, its V_O formation might be harder than that for trivalent Ln-doped samples on average as observed from H_2-TPR analysis (Figure 3).

Surface Adsorbed Species during CO Oxidation. *In situ* IR analysis of CO oxidation was performed to study the surface adsorbed species on CeO_2:Ln NWs during the catalytic process. Figure 6 shows the spectra obtained at 200 °C (see Figure S13 in SI for the spectra in other temperatures). The absorbance peaks were first divided into groups according to whether they showed the same tendency during the variation of their intensity. Then they were assigned to reported species according to their sequence in wavenumbers.[12a,28] The shape of spectra at 3800−2500 cm^{-1} was similar to the reported measurements on hydroxylated ceria surface.[28a,b] It agreed with the XPS results that hydroxyls existed on the surface according to O 1s spectra (Figure S3e and Table S8 in SI). The peaks at 3697, 3654, and 3572 cm^{-1} were attributed to the vibrations of types I, II, and III hydroxyls, respectively.[28a] The broad band around 3310 cm^{-1} increased coincidently with the peak at 1644 cm^{-1} at RT and heating-up stage. They could be assigned to bicarbonates (3310, 1644, 1378, 1216, 911 cm^{-1}).[28a,c,e] The shoulder peaks at 1577 cm^{-1} were attributed to bidentate carbonates (1577, 1286, 1064, 864 cm^{-1}).[28a,c,d] The band around 1450 cm^{-1} was approximately ascribed to the mixture of several species including unidentate carbonates (1454, 1378 cm^{-1}), inorganic carboxylates (1495 cm^{-1}), and bridged carbonates (1708, 1421, 1238 cm^{-1})[12a,28a,d,e] (Table S9 in SI). The absorbance at 2200−2100 cm^{-1} was too weak to be clearly assigned, indicating that Ce^{4+} was not the main adsorption and reaction site.[28a]

Among the above species, the absorbance of bicarbonates did not change much after 1 h isothermal at 300 °C and after cooling down to 30 °C while most of the peaks assigned to carbonates became quite weak (Figure S13c in SI). Although bicarbonates were found to be unstable for the high-temperature-calcined ceria in some reports,[28a,c] its proportion
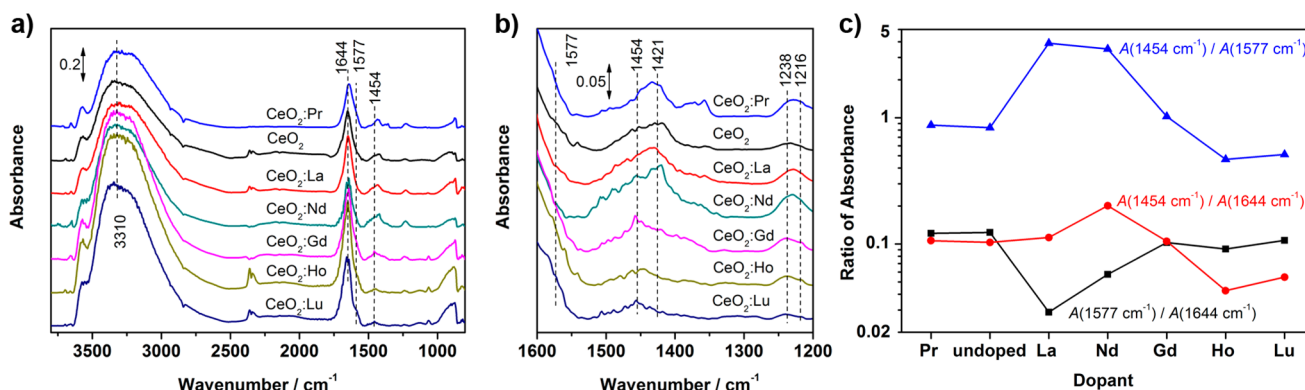
15196

dx.doi.org/10.1021/ja407616p | *J. Am. Chem. Soc.* 2013, 135, 15191−15200

Figure 6. (a) IR spectra collected during CO oxidation over CeO$_2$:Ln NWs at 200 °C. (b) Enlarged representation for selected wavenumbers in (a). (c) Variation of relative intensity at 1545, 1577, and 1644 cm^{-1} with the dopants according to the spectra in (b).

did not obviously decrease on our samples during the test. Thus, bicarbonates might be the inactive species formed during catalytic process. According to previous experimental and theoretical studies, bidentate carbonates are suggested to be the initial species for CO adsorption.[14b,28d,29] Unidentate carbonates are found to be the most active species for ceria from the mechanism study.[12a] Inorganic carboxylates had the structure that Ce or Ln directly bonded to CO$_2$. They seemed to be involved in the transfer and desorption of CO$_2$ as the products. Bridged carbonates are found to come from the adsorption of CO$_2$ according to the peak comparison of CO adsorption and CO$_2$ adsorption.[28d] Therefore, the population among bicarbonates, unidentate carbonates, and bidentate carbonates might be more important to affect the catalytic activity. For further evaluation, the bands at 1644 and 1450 cm^{-1} were fitted with Gaussian peaks. The absorbance at 1644, 1577, and 1454 cm^{-1} were measured to present the population of bicarbonates, bidentate carbonates, and unidentate carbonates, respectively. Then the ratio of absorbance for their each pair was calculated for qualitative comparisons (Figure 6c and Table S10 in SI).

The ratio of bicarbonates to both unidentate and bidentate carbonates for CeO$_2$:La was much higher than that for CeO$_2$:Nd. The relatively large proportion of inactive bicarbonates on CeO$_2$:La surface would block the active sites and become steric hindrance for the interaction of CO with lattice oxygen, leading to the decreased catalytic activity. It agreed with the above catalytic tests that CeO$_2$:La was less active than CeO$_2$:Nd. Bicarbonates may form at surface hydroxyl sites.[28a] CeO$_2$:La had the biggest ability to hydrate on its surface (see Table S8 in SI for XPS O 1s analysis) because of the smallest ionic potential for La^{3+}. Thus, the proportion of residual hydroxyls was the biggest, which resulted in the big amount of inactive bicarbonates in our temperature range (In previous study, species containing hydrogen were still detected up to about 500 °C).[12a]

The ratio of unidentate carbonates to bidentate carbonates decreased along the Ln dopant series. The sequence of this ratio was in accordance with catalytic activity sequence for most of the samples. Some reports suggest that unidentate carbonates are important species during CO oxidation and come from the conversion of bidentate carbonates.[14b,28d] Thus, the decreasing tendency to form unidentate carbonates over heavy Ln-doped ceria would result in low catalytic activity, which agreed with the results of the catalytic tests.

The special difference for valence changeable Pr-doped CeO$_2$ was more obvious at 300 °C or after cooling down to RT

(Figure S13c–d in SI). The peaks at 2848, 1566, and 1372 cm^{-1} were attributed to formates. Such species were also inactive species because their vibration bands did not disappear when cooling down to RT.

DFT simulation was carried out to study the CO adsorption and unidentate carbonates formation for CeO$_2$:Ln NWs. Because hydroxyls can hinder the CO adsorption on ceria from previous reports,[28d] the hydroxyl-free CeO$_2$:Ln (110) surface was built for the simulation. CO adsorption was simulated with the reported method.[14b,29] CO placed at O-bridge site was binded to the oxygen at NN and NNN sites next to the dopant, forming a carbonate structure with bidentate coordination (considering the limitation of our modeling, only some typical ideal configurations were simulated. There might be some possible differences in the simulated structures to the real structures assigned by IR spectra.). CO adsorption energy (E_{ads}) was calculated through eq 7:

$$E_{ads} = E(CeO_2 \text{ with } CO) - E(CeO_2) - E(CO) \qquad (7)$$

The results for some trivalent Ln-doped ceria are presented in Table S11 in SI. E_{ads} for undoped CeO$_2$ was −3.69 eV, which was similar to the reported value (−3.71 eV).[29] E_{ads} for Ln-doped CeO$_2$ was within −4.54∼−4.64 eV. The chemisorption of CO on CeO$_2$:Ln became stronger than that on undoped ceria. E_{ads} showed no obvious variation trend along the Ln dopants so the strength of CO adsorption was not the direct factor to affect the catalytic activity. Two structures containing unidentate carbonate were simulated here. The unidentate carbonate was placed at the NN site with a V$_O$ at adjacent NNN site in structure I and with no V$_O$ in structure II (Figure 7a).[14b] Previous studies have revealed that unidentate carbonates can form under CO condition, but O$_2$ is required before CO$_2$ release.[12a,24] Therefore, the conversion of the carbonate with bidentate coordination obtained from CO adsorption to unidentate carbonate structure I and its consequent conversion to structure II with the help of oxygen replenishment was calculated through the following equations:

$$\Delta E(I) = E(CeO_2 \text{ with unidentate carbonate I})$$
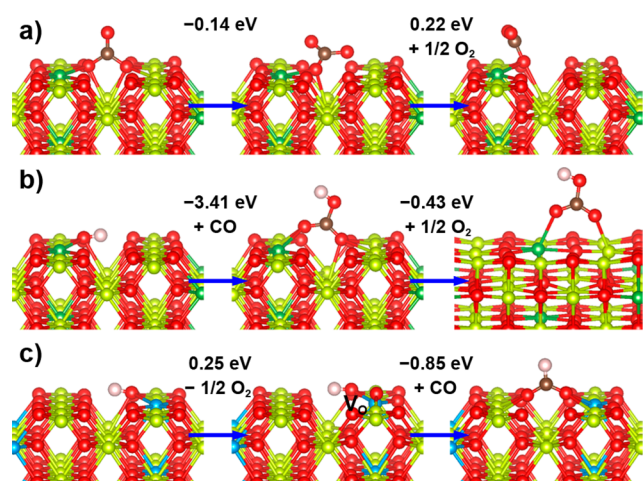$$- E(CeO_2 \text{ with bidentate carbonate}) \qquad (8)$$

Figure 7. Structures of surface species obtained from DFT simulation. (a) Evolution from CO adsorbed structure to unidentate carbonate on (110) surface exposed CeO_2:La. (b) Formation of bicarbonate on (110) surface exposed CeO_2:La. (c) Formation of formate on (110) surface exposed CeO_2:Pr. The yellow, red, green, brown, and pink balls represent Ce, O, Ln, C, and H, respectively. The structures of these species absorbed on other CeO_2:Ln were similar.

$$\Delta E(\mathrm{II}) = E(CeO_2 \text{ with unidentate carbonate II})$$
$$- E(CeO_2 \text{ with unidentate carbonate I})$$
$$- 0.5E(O_2) \qquad (9)$$

From the structures obtained from simulation in Figure 7a, the reaction in the first step could be regarded as the rotation of the carbonate from bidentate coordination to unidentate coordination which resulted in the reduced ceria surface. $\Delta E(\mathrm{I})$ was the same for each trivalent Ln-doped ceria (-0.15 ± 0.02 eV, Table S11 in SI). The second step could be regarded as the structure relaxation after oxygen replenishment. $\Delta E(\mathrm{II})$ increased from 0.22 to 0.54 eV for La–Lu-doped CeO_2, indicating that light Ln dopants were in favor of this step. In this structure, the unidentate carbonate became more close to the dopant so its property partially became similar to trivalent lanthanide carbonates: The trend of carbonates formation from oxides generally increases with the decreasing ionic potential.[30] Thus, such unidentate carbonate were easier to form on light Ln-doped CeO_2. Taking the two steps into account, both of ΔE were moderate for the supposed reaction pathway. The two steps also might be coupled because oxygen replenishment was a fast step. The total $\Delta E = \Delta E(\mathrm{I}) + \Delta E(\mathrm{II})$ had the same sequence as $\Delta E(\mathrm{II})$ did along Ln. The formation and conversion of unidentate carbonates on CeO_2:Ln were favorable on light Ln-doped ceria. It agreed with the variation trend of the proportion of unidentate carbonate species and the activity sequence for most of the samples. As for valence changeable Pr-doped ceria, $\Delta E(\mathrm{I})$ and $\Delta E(\mathrm{II})$ were 0.67 and -0.16 eV, respectively. The relative large $\Delta E(\mathrm{I})$ was unfavorable for unidentate carbonate formation, which agreed with the IR results.

Formation of bicarbonates was also calculated. One oxygen at the NN site was replaced by a hydroxyl to represent the hydrated structure. One hydrogen was bonded to each of above carbonate structures to form bicarbonates, and similar conversion process for above carbonates was calculated for bicarbonates. As Figure 7b shows, CO was possible to react with hydroxyl directly to form bicarbonates with bidentate

coordination ($\Delta E = -3.41$ eV for both CeO_2:La and CeO_2:Nd). Rearrangement process of bicarbonate together with oxygen replenishment on ceria surface was also possible to happen ($\Delta E = -0.43$ eV). Unlike the carbonate that transformed to unidentate coordination, bicarbonate still preferred bidentate coordination after structure relaxation. It would take 2.07 eV for such structure to decompose into CO_2 and H_2O, while only 1.29 eV was required for unidentate carbonate to decompose on (110) surface of CeO_2:La. It agreed with the IR results that bicarbonates were quite stable on the surfaces. Besides, bicarbonates also might form through the acid–basic reaction between hydroxyls and CO_2 ($\Delta E = -0.60$ eV). Therefore, the relatively large amount of hydroxyls on CeO_2:La could easily convert to inactive bicarbonates, leading to decreased activity.

The formation mechanism of formates has been suggested to be the reaction of CO at V_O site with adjacent hydroxyl.[28b] Such reactions were simulated for CeO_2:Pr, CeO_2:La, and undoped CeO_2 (Figure 7c). One hydroxyl was placed at NN site to the surface dopant. Formation energy of V_O at its adjacent NN site was calculated. It was 0.25, 0.35, and 1.74 eV for CeO_2:Pr, CeO_2:La, and undoped ceria, respectively, which was similar to the V_O formation energy on hydroxyl-free surfaces. CO adsorption energies at such sites to form formates were -0.85, -1.25, and -1.62 eV on CeO_2:Pr, CeO_2:La, and undoped CeO_2, respectively. There seemed to be no obvious enhanced tendency of formates formation on Pr uniformly doped ceria compared to that on trivalent La-doped ceria. Besides, hydroxyls on CeO_2:La were more possible to turn into bicarbonates according to above calculations (-3.41 eV). Such conversion to bicarbonates required -2.70 eV on CeO_2:Pr, indicating that bicarbonates were also easier to form at hydroxyl sites rather than formates on uniformly doped CeO_2:Pr. Therefore, the inactive formates were most probably attributed to the surface heterogeneity on CeO_2:Pr samples, which were hard to simulate here. From this aspect, it became another advantage for our uniformly doped samples to avoid unexpected side reactions.

To sum up, in the present research, the correlation between catalytic activity variation and Ln dopants in CO oxidation were demonstrated through two main pathways: direct oxidation of CO with lattice oxygen and surface process involving the formation and conversion of coordinated carbonate species. For CeO_2:Ln NWs, V_O formation ability and the bonding modes of surface species involved in the catalytic process could accordingly affect the above two pathways, leading to the variation in catalytic activity along the Ln dopants. V_O formation ability had a positive relation to the distortion around Ln dopants. The bonding configuration of surface species was affected by the ionic potential of the dopants. Thus, such factors and the catalytic activity were sensitive to the ionic radius of the dopants. The relatively large amount of inactive bicarbonates on CeO_2:La might block the active sites and became steric hindrance for CO to approach active centers. Thus, CeO_2:La showed lower catalytic activity than CeO_2:Nd, although its V_O formation energy was lower. V_O formation became harder from CeO_2:La to CeO_2:Ho and then became easier to CeO_2:Lu. The proportion of active unidentate carbonates decreased on heavy Ln-doped samples. Therefore, the catalytic activity decreased from CeO_2:Nd to CeO_2:Dy and was similar for CeO_2:Dy–CeO_2:Lu, and Nd-doped CeO_2 NWs showed the best catalytic activity. For most of the lanthanide dopants, these two factors resulted in similar variation trend in

determining their reactivity sequences. The surface micro-structure heterogeneity in valence changeable Pr-doped CeO_2 caused decreased V_O formation tendency on average and led to the formation of inactive formates on surfaces during catalysis, which resulted in low catalytic activity.

CONCLUSIONS

Lanthanide uniformly doped CeO_2 NWs with no residual capping agents were prepared by controlling the redox property of Ce(III)/Ce(IV) in the hydrothermal synthesis. Structure distortion around the dopants altered with varied Ln dopants, which was verified through EXAFS analysis. The catalytic activity of CeO_2:Ln NWs was improved with respect to the undoped samples because of the activated surface oxygen and the enhanced CO chemisorption ability due to the introduction of the Ln_{Ce}' defects. When the lanthanide dopants were varied, the CO oxidation reactivity over CeO_2:Ln NWs increased from CeO_2:La to CeO_2:Nd and decreased from CeO_2:Sm to CeO_2:Lu. Nd-doped samples showed the best catalytic activity; whereas valence changeable Ln ion doped samples gave worse catalytic performance than other trivalent Ln ion doped ones. Experimental observations demonstrated two factors that influenced such variation trend: oxygen release ability and the population of surface adsorbed active unidentate carbonates and inactive bicarbonates formed during CO oxidation. The relative large ratio of inactive bicarbonates limited the activity of CeO_2:La. The decreasing V_O formation tendency and decreasing population of active unidentate carbonates over heavy Ln-doped ceria NWs caused the decreasing reactivity for CeO_2:Sm−CeO_2:Lu. DFT simulation further suggested that the enhanced V_O formation ability exhibited a positive relation to the increased structure disorder around the dopants including lattice expansion and contraction. The population of carbonate species on CeO_2:Ln was correlated to the ionic potential of the dopants. Therefore, CO oxidation reactivity over CeO_2:Ln NWs was sensitive to the ionic radius of Ln dopants. This work not only indicated that doping foreign ions into host catalysts could modify the active site structures as well as the surface bonding modes of reactive intermediates but also suggested that a moderate range of ionic radius of dopants might exist for improving catalytic activities of composite nanocatalysts for high-efficiency nanocatalysis.

ASSOCIATED CONTENT

Ⓢ Supporting Information

XRD patterns, EXAFS spectra, more TEM images and catalytic properties, and other data. This material is available free of charge via the Internet at http://pubs.acs.org.

AUTHOR INFORMATION

Corresponding Authors
ywzhang@pku.edu.cn
hcliu@pku.edu.cn
yan@pku.edu.cn

Author Contributions
⊥These authors contributed equally.

Notes
The authors declare no competing financial interest.

ACKNOWLEDGMENTS

REFERENCES

(1) (a) Thomas, J. M. *Angew. Chem., Int. Ed.* **1999**, *38*, 3588. (b) Hutchings, G. J. *J. Mater. Chem.* **2009**, *19*, 1222. (c) Nørskov, J. K.; Bligaard, T.; Rossmeisl, J.; Christensen, C. H. *Nat. Chem.* **2009**, *1*, 37. (d) Rodriguez, J. A. *Theor. Chem. Acc.* **2002**, *107*, 117.

(2) (a) Philippot, K.; Serp, P. Concepts in nanocatalysis. In *Nanomaterials in Catalysis*; Wiley-VCH: Weinheim, 2013; Chpt. 1. (b) Copéret, C.; Chabanas, M.; Saint-Arroman, R. P.; Basset, J.-M. *Angew. Chem., Int. Ed.* **2003**, *42*, 156. (c) Astruc, D.; Lu, F.; Aranzaes, J. R. *Angew. Chem., Int. Ed.* **2005**, *44*, 7852. (d) Bäckvall, J.-E. *Top. Catal.* **2010**, *53*, 831. (e) Corma, A.; Garcia, H. *Top. Catal.* **2008**, *48*, 8. (f) Somorjai, G. A.; Frei, H.; Park, J. Y. *J. Am. Chem. Soc.* **2009**, *131*, 16589.

(3) (a) Zhou, K.; Li, Y. *Angew. Chem., Int. Ed.* **2012**, *51*, 602. (b) Gu, J.; Zhang, Y.-W.; Tao, F. *Chem. Soc. Rev.* **2012**, *41*, 8050. (c) Lee, I.; Delbecq, F.; Morales, R.; Albiter, M. A.; Zaera, F. *Nat. Mater.* **2009**, *8*, 132. (d) Crespo-Quesada, M.; Yarulin, A.; Jin, M.; Xia, Y.; Kiwi-Minsker, L. *J. Am. Chem. Soc.* **2011**, *133*, 12787.

(4) Bhattacharjee, S.; Dotzauer, D. M.; Bruening, M. L. *J. Am. Chem. Soc.* **2009**, *131*, 3601.

(5) (a) Yamada, Y.; Tsung, C.-K.; Huang, W.; Huo, Z.; Habas, S. E.; Soejima, T.; Aliaga, C. E.; Somorjai, G. A.; Yang, P. *Nat. Chem.* **2011**, *3*, 372. (b) Xing, Y.; Cai, Y.; Vukmirovic, M. B.; Zhou, W.-P.; Karan, H.; Wang, J. X.; Adzic, R. R. *J. Phys. Chem. Lett.* **2010**, *1*, 3238. (c) Guo, X.; Fu, Q.; Ning, Y.; Wei, M.; Li, M.; Zhang, S.; Jiang, Z.; Bao, X. *J. Am. Chem. Soc.* **2012**, *134*, 12350.

(6) (a) Zafeiratos, S.; Piccinin, S.; Teschner, D. *Catal. Sci. Technol.* **2012**, *2*, 1787. (b) Behrens, M.; Studt, F.; Kasatkin, I.; Kühl, S.; Hävecker, M.; Abild-Pedersen, F.; Zander, S.; Girgsdies, F.; Kurr, P.; Kniep, B.-L.; Tovar, M.; Fischer, R. W.; Nørskov, J. K.; Schlögl, R. *Science* **2012**, *336*, 893.

(7) (a) Gross, E.; Liu, J. H.-C.; Toste, F. D.; Somorjai, G. A. *Nat. Chem.* **2012**, *4*, 947. (b) Qiao, B.; Wang, A.; Yang, X.; Allard, L. F.; Jiang, Z.; Cui, Y.; Liu, J.; Li, J.; Zhang, T. *Nat. Chem.* **2011**, *3*, 634. (c) Park, J. B.; Graciani, J.; Evans, J.; Stacchiola, D.; Ma, S.; Liu, P.; Nambu, A.; Sanz, J. F.; Hrbek, J.; Rodriguez, J. A. *Proc. Natl. Acad. Sci. U.S.A.* **2009**, *106*, 4975. (d) Bruix, A.; Rodriguez, J. A.; Ramírez, P. J.; Senanayake, S. D.; Evans, J.; Park, J. B.; Stacchiola, D.; Liu, P.; Hrbek, J.; Illas, F. *J. Am. Chem. Soc.* **2012**, *134*, 8968.

(8) (a) Vattuone, L.; Savio, L.; Rocca, M. *Surf. Sci. Rep.* **2008**, *63*, 101. (b) Si, R.; Zhang, Y.-W.; Wang, L.-M.; Li, S.-J.; Lin, B.-X.; Chu, W.-S.; Wu, Z.-Y.; Yan, C.-H. *J. Phys. Chem. C* **2007**, *111*, 787.

(9) Thomas, J. M.; Raja, R.; Lewis, D. W. *Angew. Chem., Int. Ed.* **2005**, *44*, 6456.

(10) (a) Royer, S.; Duprez, D. *ChemCatChem* **2011**, *3*, 24. (b) Paier, J.; Penschke, C.; Sauer, J. *Chem. Rev.* **2013**, *113*, 3949. (c) Xie, X.; Li, Y.; Liu, Z.-Q.; Haruta, M.; Shen, W. *Nature* **2009**, *458*, 746.

(11) (a) Trovarelli, A. *Catal. Rev.: Sci. Eng.* **1996**, *38*, 439. (b) Glaspell, G.; Hassan, H. M. A.; Elzatahry, A.; Abdalsayed, V.; El-Shall, M. S. *Top. Catal.* **2008**, *47*, 22. (c) Feng, L.; Hoang, D. T.; Tsung, C.-K.; Huang, W.; Lo, S. H.-Y.; Wood, J. B.; Wang, H.; Tang, J.; Yang, P. *Nano Res.* **2011**, *4*, 61. (d) Si, R.; Flytzani-Stephanopoulos, M. *Angew. Chem.* **2008**, *120*, 2926. (e) Ta, N.; Liu, J.; Chenna, S.; Crozier, P. A.; Li, Y.; Chen, A.; Shen, W. *J. Am. Chem. Soc.* **2012**, *134*, 20585. (f) Vivier, L.; Duprez, D. *ChemSusChem* **2010**, *3*, 654.

(12) (a) Wu, Z.; Li, M.; Overbury, S. H. *J. Catal.* **2012**, *285*, 61. (b) Wu, Z.; Li, M.; Howe, J.; Meyer, H. M., III; Overbury, S. H.

Langmuir **2010**, *26*, 16595. (c) Nolan, M.; Parker, S. C.; Watson, G. W. *Surf. Sci.* **2005**, *595*, 223.

(13) (a) Mai, H.-X.; Sun, L.-D.; Zhang, Y.-W.; Si, R.; Feng, W.; Zhang, H.-P.; Liu, H.-C.; Yan, C.-H. *J. Phys. Chem. B* **2005**, *109*, 24380. (b) Pan, C.; Zhang, D.; Shi, L.; Fang, J. *Eur. J. Inorg. Chem.* **2008**, *15*, 2429. (c) Wang, D.; Kang, Y.; Doan-Nguyen, V.; Chen, J.; Küngas, R.; Wieder, N. L.; Bakhmutsky, K.; Gorte, R. J.; Murray, C. B. *Angew. Chem., Int. Ed.* **2011**, *50*, 4378. (d) Liu, X.; Zhou, K.; Wang, L.; Wang, B.; Li, Y. *J. Am. Chem. Soc.* **2009**, *131*, 3140. (e) Lawrence, N. J.; Brewer, J. R.; Wang, L.; Wu, T.-S.; Wells-Kingsbury, J.; Ihrig, M. M.; Wang, G.; Soo, Y.-L.; Mei, W.-N.; Cheung, C. L. *Nano Lett.* **2011**, *11*, 2666. (f) Si, R.; Zhang, Y.-W.; Li, S.-J.; Lin, B.-X.; Yan, C.-H. *J. Phys. Chem. B* **2004**, *108*, 12481. (g) Ahn, K.; Yoo, D. S.; Prasad, D. H.; Lee, H.-W.; Chung, Y.-C.; Lee, J.-H. *Chem. Mater.* **2012**, *24*, 4261. (h) Małecka, M. A.; Kępiński, L.; Miśta, W. *J. Am. Ceram. Soc.* **2008**, *451*, 567.

(14) (a) Hu, Z.; Metiu, H. *J. Phys. Chem. C* **2011**, *115*, 17898. (b) Yeriskin, I.; Nolan, M. *J. Chem. Phys.* **2009**, *131*, 244702. (c) Yeriskin, I.; Nolan, M. *J. Phys.: Condens. Matter* **2010**, *22*, 135004. (d) Kehoe, A. B.; Scanlon, D. O.; Watson, G. W. *Chem. Mater.* **2011**, *23*, 4464.

(15) Hernández, W. Y.; Laguna, O. H.; Centeno, M. A.; Odriozola, J. A. *J. Solid State Chem.* **2011**, *184*, 3014.

(16) Yamazaki, S.; Matsui, T.; Ohashi, T.; Arita, Y. *Solid State Ionics* **2000**, *136*, 913.

(17) Castleton, C. W.; Kullgren, J.; Hermansson, K. *J. Chem. Phys.* **2007**, *127*, 244704.

(18) Jiang, H.; Gomez-Abal, R. I.; Rinke, P.; Scheffler, M. *Phys. Rev. Lett.* **2009**, *102*, 126403.

(19) Lange, N. A.; Dean, J. A. *Lange's Handbook of Chemistry*, 13th ed.; McGraw-Hill: New York, 1985.

(20) Shannon, R. D. *Acta Crystallogr., Sect. A* **1976**, *32*, 751.

(21) Brice, J. C. *J. Cryst. Growth* **1975**, *28*, 249.

(22) Madier, Y.; Descorme, C.; Le Govic, A. M.; Duprez, D. *J. Phys. Chem. B* **1999**, *103*, 10999.

(23) (a) Nörenberg, H.; Briggs, G. A. D. *Surf. Sci.* **1999**, *433*, 127. (b) Sayle, D. C.; Maicaneanu, S. A.; Watson, G. W. *J. Am. Soc. Chem.* **2002**, *124*, 11429.

(24) (a) Aneggi, E.; Boaro, M.; de Leitenberg, C.; Dolcetti, G.; Trovarelli, A. *J. Alloy. Compd.* **2006**, *408*, 1096. (b) Boaro, M.; Giordano, F.; Recchia, S.; Dal Santo, V.; Giona, M.; Trovarelli, A. *Appl. Catal., B* **2004**, *52*, 225.

(25) Yao, H. C.; Yao, Y. F. Y. *J. Catal.* **1984**, *86*, 254.

(26) Ma, L.; Chen, W.-X.; Zhao, J.; Zheng, Y.-F. *J. Cryst. Growth* **2007**, *303*, 590.

(27) Nolan, M. *J. Phys. Chem. C* **2011**, *115*, 6671.

(28) (a) Pozdnyakova, O.; Teschner, D.; Wootsch, A.; Kröhnert, J.; Steinhauer, B.; Sauer, H.; Toth, L.; Jentoft, F. C.; Knop-Gericke, A.; Paál, Z.; Schlögl, R. *J. Catal.* **2006**, *237*, 1. (b) Li, C.; Sakata, Y.; Arai, T.; Domen, K.; Maruya, K.; Onishi, T. *J. Chem. Soc., Faraday Trans. 1* **1989**, *85*, 1451. (c) Finos, G.; Collins, S.; Blanco, G.; del Rio, E.; Cíes, J. M.; Bernal, S.; Bonivardi, A. *Catal. Today* **2012**, *180*, 9. (d) Li, C.; Sakata, Y.; Arai, T.; Domen, K.; Maruya, K.; Onishi, T. *J. Chem. Soc., Faraday Trans. 1* **1989**, *85*, 929. (e) Jin, T.; Zhou, Y.; Mains, G. J.; White, J. M. *J. Phys. Chem.* **1987**, *91*, 5931.

(29) Huang, M.; Fabris, S. *J. Phys. Chem. C* **2008**, *112*, 8643.

(30) Atkins, P. W.; Overton, T. L.; Rourke, J. P.; Weller, M. T.; Armstrong, F. A. *Shriver and Atkins' Inorganic Chemistry*, 5th Ed.; Oxford University Press: Oxford, 2009.